Available online at www.sciencedirect.com
SCIENCE DIRECT®
Journal of Power Sources 123 (2003) 79–85
JOURNAL OF POWER SOURCES
www.elsevier.com/locate/jpowsour

Review

Electrochemical capacitor performance of hydrous ruthenium oxide/mesoporous carbon composite electrodes

Jong H. Jang, Sangjin Han, Taeghwan Hyeon, Seung M. Oh*

School of Chemical Engineering and Research Center for Energy Conversion and Storage, Seoul National University, Seoul 151-744, South Korea

Received 11 February 2003; accepted 17 March 2003

Abstract

Ruthenium/carbon composite materials are prepared by impregnating ruthenium(III) acetylacetonate into a mesoporous carbon (average pore diameter = 12 mn, pore volume = 3.6 $cm^3 g^{-1}$) and then heat treatment at 320 °C for 2 h under an argon atmosphere. The metallic ruthenium nanoparticles are converted to pseudo-capacitive hydrous ruthenium oxide by electrochemical oxidation at 0.75 V (versus SCE) for 2 h in 2.0 M H_2SO_4. The specific capacitance of the composite electrodes, which is the sum of the double-layer capacitance of mesoporous carbon and the pseudo-capacitance of hydrous ruthenium oxide, reaches 243 F g^{-1} with heavy loading. As the loading is increased, however, the degree of ruthenium utilization for a pseudo-capacitor becomes poorer, presumably due to a limited conversion to the hydrous oxide form. The rate capability of composite electrodes also decreases with increase in ruthenium loading, due to an increase in both the equivalent series resistance (ESR) and the overall capacitance value.

The ESR enlargement is caused mainly an increase in the electrolyte resistance within pores which, in turn, results from a pore narrowing with ruthenium loading Hindered ionic motion in narrowed pores can explain this feature. An increase in the *RC* time constant with ruthenium loading is further verified by ac impedance measurements.

Keywords: Electrochemical capacitors; Mesoporous carbons; Pseudo-capacitance; Hydrous ruthenium oxides; AC impedance spectroscopy

1. Introduction

Electrochemical capacitors have been considered as a promising high-power sources for digital communication devices and electric vehicles. The advantageous features of electrochemical capacitors are superior rate capability and longer cycle-life compared with modern secondary batteries. Electrochemical capacitors may be classified into two groups, namely, electric double-layer capacitors (EDLC) and pseudo-capacitors (PC) [1]. The former stores electric charges at the double-layer formed at electrode|electrolyte interface. In the latter, electric charges are stored mainly in the electrode surface region by faradaic reactions.

At present, activated carbons are the favored choice of EDLC electrode materials. Even if these carbons have a sufficiently large surface area, their application in EDLC capacitors is rather limited because they contain pores that range in size from micropores (<2 nm diameter) to macropores. The micropores are less easily wetted by electrolytes, such that the surface exposed may not be utilized for charge storage. Moreover, even in a situation where the micropores are wetted by electrolytes, ionic motion in such small pores is not facilitated, such that the high-rate capability, which is one of the inherent advantages of EDLCs, may not be realized [2]. Carbon aerogels or xerogels that carry larger pores have become popular as an alternative EDLC material [3–6].

One of the drawbacks of carbon-based EDLCs is their low specific energy density compared with that of modern secondary batteries. One approach to enhance the specific energy is the addition of a pseudo-capacitor component into EDLC electrodes [7–11]. For this purpose, hydrous ruthenium oxide is most commonly employed [12].

The preparation of hydrous ruthenium oxide/carbon composites has been reported by other workers. Miller and co-workers [13–15] prepared the ruthenium/carbon aerogel by chemical vapor impregnation of ruthenium(III) acetylacetonate into carbon aerogels. In a different approach, Lin et al. [16] synthesized a similar composite material by adding $RuO_x \cdot H_2O$ powder in the sol–gel resorcinol formaldehyde resin formation reaction and subsequent carbonization at 750 °C in a nitrogen atmosphere. In both syntheses, the ruthenium nanoparticles were activated to the pseudo-capacitive hydrous oxide form by an

* Corresponding author. Tel.: +82-2-880-7074; fax: +82-2-872-5755.
E-mail address: seungoh@plaza.snu.ac.kr (S.M. Oh).

0378-7753/$ – see front matter © 2003 Elsevier Science B.V. All rights reserved.
doi:10.1016/S0378-7753(03)00459-2

electrochemical oxidation. In the present work, hydrous ruthenium oxide/carbon composite electrode materials are prepared according to the method adopted by Miller et al. A mesoporous carbon, instead of carbon aerogels, is used and has a uniform pore-size of 12 nm, a surface area of 570 $m^2\,g^{-1}$, and a pore volume of 3.6 $cm^3\,g^{-1}$.

The previous studies [13–16] demonstrated capacitance enhancement by adding a hydrous ruthenium oxide component into the carbon electrode. An important issue here is, however, the extent of ruthenium utilization as a pseudo-capacitor according to the loading. Practically, a maximum utilization rather than heavy loading is desirable because ruthenium is an expensive material. This, therefore, is the prime objective of the present study. The capacitance increase with ruthenium loading is also likely counterbalanced by a loss of rate capability because ionic motions may be less facilitated due to a pore narrowing with loading. This issue is also addressed.

2. Experimental

2.1. Materials

The synthesis of mesoporous carbon has been reported earlier [17]. The ruthenium nanoparticles were loaded on to the mesoporous carbon by a chemical vapor impregnation method [13]. For the preparation, a mixture of mesoporous carbon and ruthenium(III) acetylacetonate (Aldrich) was placed in a round-bottom flask. Under static vacuum conditions, the ruthenium compound was sublimated by heating at 190 °C. Then, the mixture was cooled down to room temperature to maximize the infiltration of ruthenium compound into the carbon pores. The impregnated ruthenium(III) acetylacetonate was thermally decomposed into metallic Ru by heating at 320 °C for 2 h under an argon atmosphere. The ruthenium loading was controlled either by adjusting the ruthenium(III) acetylacetonate/carbon weight ratio or by repeating the impregnation/decomposition procedure several times.

The surface area and pore-size distribution were calculated from nitrogen adsorption isotherms (Micrometrics ASAP 2010) using the Brunauer, Emmett, and Teller (BET), and Barrett, Joyner, and Halenda (BJH) methods, respectively. The content of ruthenium in the composites was estimated by means of thermogravimetric analysis (TGA, Perkin-Elmer TGA7). X-ray diffraction (XRD) patterns were obtained with a MacScience M18XHF diffractometer with Cu Kα radiation ($\lambda = 0.15418$ nm). Transmission electron microscopic (TEM) images were obtained with a Phillips CM-20 instrument.

2.2. Electrochemical characterizations

The electrochemical capacitor performance of the composite electrodes was analyzed with a three-electrode configuration in a beaker-type cell. To prepare the working electrode, the mixture of composite powder, polytetrafluoroethylene (PTFE) binder and conducting aid (Ketjenblack ECP-600JD) was dispersed in isopropyl alcohol and coated on a stainless-steel mesh (apparent area = 2 cm^2). The resulting electrode was pressed and dried under vacuum. The amount of conducting agent was controlled for all the electrodes to have the same electrode resistance. A platinum flag and a saturated calomel electrode (SCE) were used as the counter and reference electrodes, respectively. The electrolyte was 2.0 M H_2SO_4 aqueous solution. Prior to electrochemical characterization, metallic ruthenium in the composite electrodes was converted to the hydrous oxide form by electrochemical oxidation at 0.75 V (versus SCE) for 2 h [18–20]. The specific capacitance of each composite electrode steadily increased according to the electrochemical oxidation time, indicative of a gradual conversion from metallic ruthenium to a hydrous oxide form, but reached a maximum steady value within 2 h. Therefore, the electrochemical oxidation time was fixed for 2 h for all the samples. Cyclic voltammetry and galvanostatic charge–discharge cycling were performed with a EG&G PARC 362 potentiostat in the potential range −0.1 to 0.8 V (versus SCE). Electrochemical impedance measurements were made over the frequency range 10^6 to 5×10^{-3} Hz (Zahner, im6e).

3. Results and discussion

3.1. Material characterizations

The loading of ruthenium was estimated from the residue content after charring the composite materials in air. The TGA results are presented in Fig. 1. The mesoporous carbon and ruthenium/mesoporous carbon composite materials were designated RV0 to RV4 according to their residue content. RV0 represents the unloaded mesoporous carbon. As

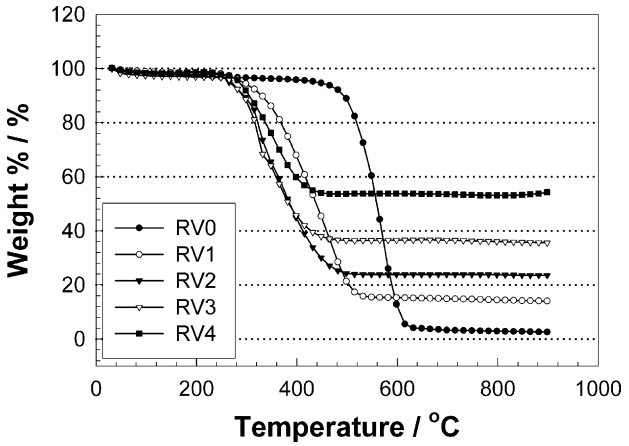

Fig. 1. Thermogravimetric analysis (TGA) data of mesoporous carbon and ruthenium/mesoporous carbon composites. For the unloaded carbon (RV0), the residue content was 2.6 wt.% after charring up to 900 °C.

Table 1
Characteristics of mesoporous carbon and ruthenium/mesoporous carbon composite electrodes

	Residue (wt.%)[a]	Surface area ($m^2\,g^{-1}$)	Total specific capacitance (C_{sp}, $F\,g^{-1}$)	Specific capacitance of Ru component (C_{sp}^{Ru}, $F\,g^{-1}$)
RV0	2.6	570	100	–
RV1	14.0	535	177	738
RV2	23.5	521	174	448
RV3	35.6	406	184	346
RV4	54.3	286	243	363

[a] The major component of residue appears to be ruthenium but a minor amount of inorganic impurity cannot be ignored.

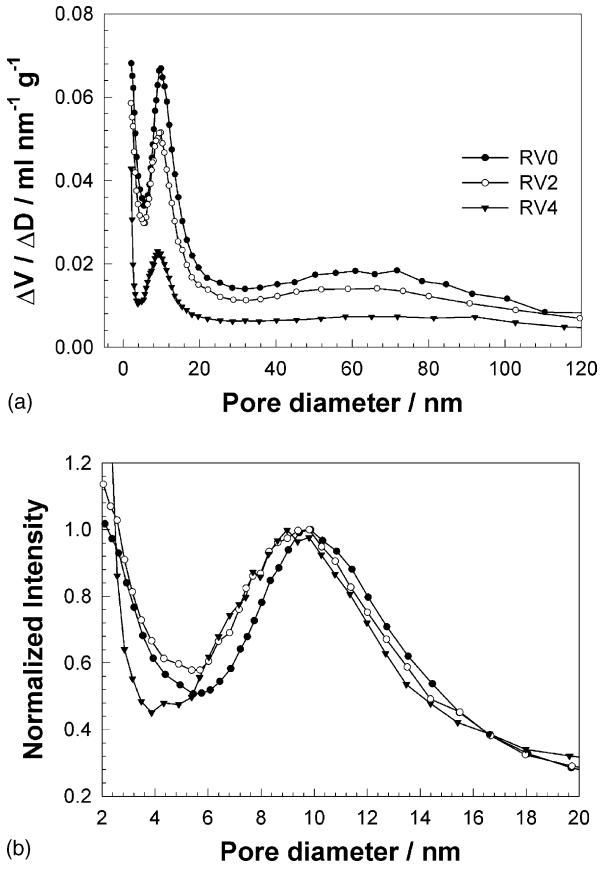

Fig. 2. (a) Pore-size distribution of the mesoporous carbon (RV0) and ruthenium/mesoporous carbon composites (RV2 and RV4). (b) normalized pore-size distribution emphasizing the mesopore region. Note a slight, but apparent, pore narrowing with ruthenium loading.

listed in Table 1, this mesoporous carbon has a residue content of 2.6 wt.%, which comes from inorganic impurities. The ruthenium loading is highest in the RV4 sample, viz. 54.3 wt.%. In the TGA profiles, the weight loss (carbon oxidation) of ruthenium-loaded samples occurs at lower temperatures than that for the pure mesoporous carbon because of the catalytic effects of ruthenium species for carbon gasification [21,22].

The mesoporous carbon has a narrow pore-size distribution with a peak value of 10 nm (Fig. 2). The BET surface area is $570\,m^2\,g^{-1}$, and the BJH cumulative pore volume (corresponding to pores >2 nm) is as high as $3.6\,cm^3\,g^{-1}$. The BET surface-area decreases as the ruthenium loading increases (Table 1) because this parameter is normalized per unit weight. The pore structure of mesoporous carbon does not change substantially with ruthenium loading, but the peak around 10 nm is shifted to the smaller size direction, indicative of a slight pore narrowing with ruthenium loading (Fig. 2b).

The TEM photographs (Fig. 3) reveal that ruthenium nanoparticles are deposited on the surface of mesoporous carbon. For samples with higher loadings, the number of ruthenium particles increases with a slight size enlargement.

In the XRD patterns (Fig. 4), the mesoporous carbon (RV0) shows broad diffraction peaks at $2\theta = 24$ and 43° that are related to the (0 0 2) and (1 0 0) reflections of microcrystalline carbon, respectively [23]. With ruthenium loading, the diffraction peaks of metallic ruthenium (JCPDS No. 06–0663) develop as marked with bars, a feature which is due to thermal decomposition of ruthenium acetylacetonate [24,25]. Even if the diffraction peaks of metallic ruthenium

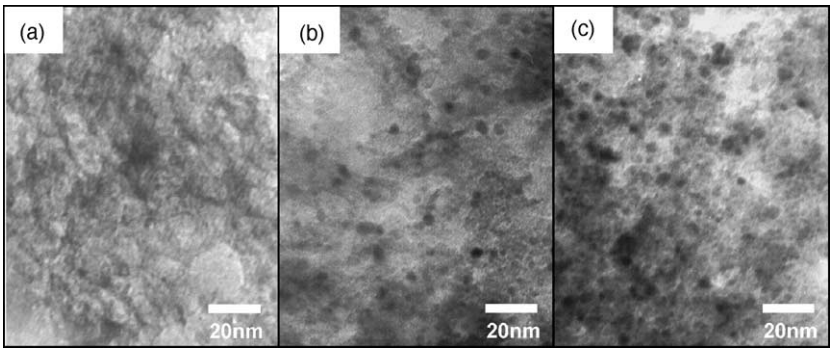

Fig. 3. TEM photographs of mesoporous carbon and ruthenium-loaded mesoporous carbon composites: (a) RV0; (b) RV2; (c) RV4. Ruthenium nanoparticles (particle size <10 nm) are evenly distributed. For the sample with a higher loading (RV4), a slight size increment with agglomeration is observed.

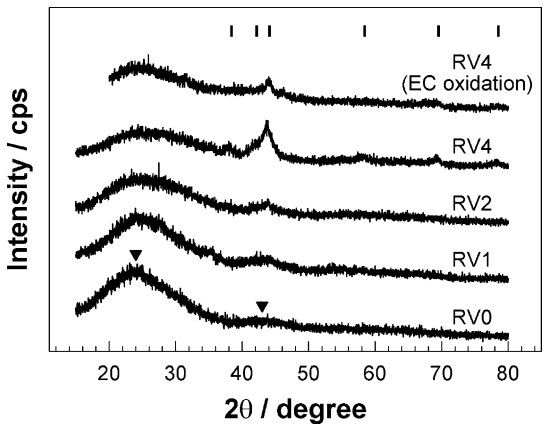

Fig. 4. XRD patterns of ruthenium/mesoporous carbon composites. The filled triangle and vertical bar locate the diffraction peaks of microcrystalline carbon and metallic ruthenium, respectively. The top profile is the XRD profile taken after electrochemical oxidation of RV4 at 0.75 V (vs. SCE) for 2 h.

are broad and weak, they become more intense with increase in ruthenium loading. In particular, note the steady intensity growth of the peak appearing at 44° that is related to the (1 0 1) diffraction of metallic Ru.

3.2. Electrochemical capacitor performance

The cyclic voltammograms for RV0, RV2 and RV4 electrodes are shown in Fig. 5. All the electrodes display a capacitive charging current in both scanning directions across the potential range −0.1 to 0.8 V (versus SCE). In the case of the pristine carbon electrode (RV0), however, a redox current peak near 0.3 V is present, which comes from the charge-transfer reaction at the surface quinone/hydroquinone groups [26,27]. In concept with the ruthenium loading, the capacitive current becomes larger, which is the result of a contribution from the pseudo-capacitive hydrous ruthenium oxide component [13–16].

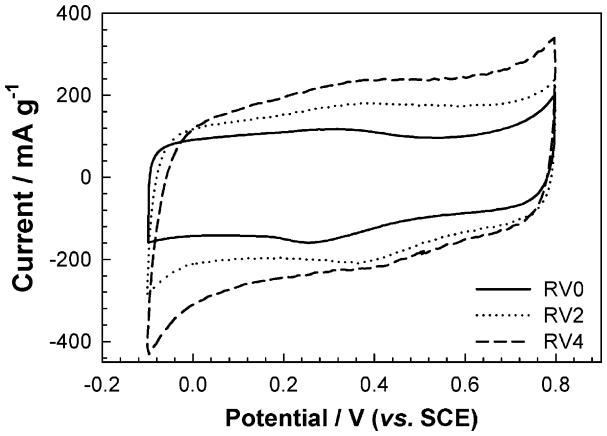

Fig. 5. Cyclic voltammograms for RV0, RV2 and RV4 electrodes. The scan rate is 1 mV s^{-1}.

The total specific capacitance (C_{sp}) with respect to ruthenium loading is listed in Table 1. The specific capacitance was calculated from the equation, $C_{sp} = I/(\nu \times m)$, where I is the current in the cyclic voltammogram ν the scan rate, and m the mass of the composite materials. The current values at 0.6 V in the positive-going scan were taken for the calculation. The unloaded mesoporous carbon delivers a specific capacitance of 100 F g^{-1}, but increases with ruthenium loading, to reach 243 F g^{-1} at 54.3 wt.% loading (RV4).

Utilization of the ruthenium component in the composite electrodes is an important aspect for practical applications. To evaluate the degree of ruthenium utilization, a new parameter (C_{sp}^{Ru}) is introduced. This is calculated by dividing the capacitance delivered from hydrous ruthenium oxide by its weight. For the calculation, the following assumptions are made: (i) the total capacitance of composite electrodes is the sum of two capacitances; (ii) the specific capacitance of carbon itself is not affected by the ruthenium loading. The latter assumption is valid since only a small fraction of the carbon surface is covered by ruthenium particles (Fig. 3). In Fig. 6, the C_{sp}^{Ru} along with the specific capacitance delivered by the carbon and ruthenium components are plotted according to the ruthenium loading; the data are listed in Table 1. The capacitance contributed by the mesoporous carbon steadily decreases with increasing 'ruthenium content' because the numbers are normalized by the total weight of the composite materials. That is, the absolute amount of the carbon component in the composites becomes smaller with ruthenium loading. The C_{sp}^{Ru} of RV1 electrode is 738 F g^{-1}, which is comparable with that of amorphous hydrous ruthenium oxide (760 F g^{-1}). [12]. As the ruthenium loading increases, however; the C_{sp}^{Ru} decreases down to 346 F g^{-1}. The smaller C_{sp}^{Ru} in the heavily-loaded electrodes indicates that the ruthenium component is not fully utilized for charge storage. This feature likely originates from an incomplete conversion of metallic ruthenium to hydrous Ru oxide in the electrochemical oxidation step, which is ascertained from the XRD data shown in Fig. 4. The top profile in Fig. 4 was taken after electrochemical oxidation of the RV4 sample at 0.75 V (versus SCE) for 2 h. As seen, the diffraction peaks associated with metallic ruthenium still remain even after the electrochemical treatment. It should be pointed out that, even if the electrochemical oxidation time is extended for >2 h, the conversion yield is not improved. It is likely that the electrochemical oxidation starts from the surface of the ruthenium particle and the oxidation rate becomes slower as the reaction proceeds. As a consequence, smaller particles may be fully oxidized and thus utilized as a pseudo-capacitor. The C_{sp}^{Ru} of RV1 electrode, which approaches the theoretical value of hydrous ruthenium oxide, may explain this feature. In the case of larger ruthenium particles, however, only the surface region is oxidized. Actually, the heavily loaded electrode (RV4) exhibits a significantly reduced utilization of ruthenium.

The specific capacitance versus potential profiles as a function of scan rate are shown in Fig. 7. The profiles were

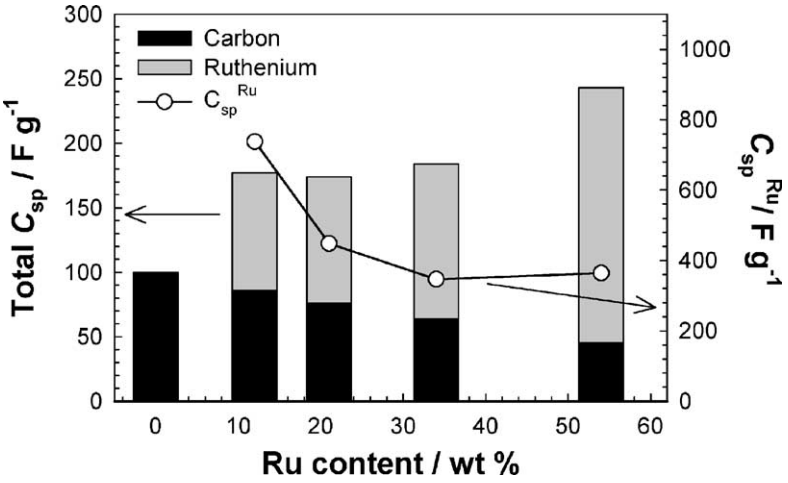

Fig. 6. Specific capacitance delivered by carbon and ruthenium components, and specific capacitance of ruthenium component (C_{sp}^{Ru}) as a function of ruthenium loading.

obtained by dividing the current in cyclic voltammograms by the scan rate. At a slow scan (1 mV s^{-1}), the profiles of the three electrodes have rectangular-like shapes. As the scan rate increases, however, the profiles become gradually depressed. It is also noted that the depression is more pronounced in the highly-loaded electrode. The degree of depression can be correlated with the rate capability of the electrode system which, in turn, is deeply related to the *RC* time constant. That is, if any capacitor system has a large *RC* time constant, the rate capability is poor. This feature is ascertained by the profiles shown in Fig. 7, whereby the exponential transient appearing before the plateau becomes longer because more time is required to charge the capacitor [28]. Here, *R* and *C* denote the equivalent series resistance (ESR) and capacitance, respectively. The ESR is the summation of electrode resistance, bulk electrolyte resistance and electrolyte resistance within pores. The poorer rate capability observed with highly-loaded electrodes is caused by a larger value of either capacitance or ESR. The cause is clear in the case of the larger capacitance with heavier Ru loading. An increase in ESR with ruthenium loading is visually seen in the galvanostatic charge–discharge profiles shown in Fig. 8, where the voltage drop at the very earlier period of charge–discharge switching is noticed. A careful inspection

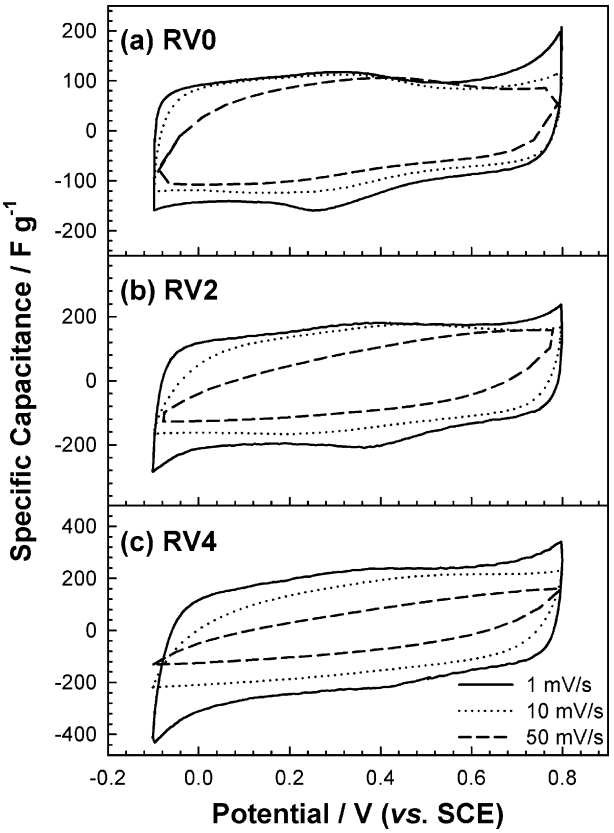

Fig. 7. Specific capacitance (C_{sp}) vs. potential plots of three electrodes as a function of scan rate. Note a pronounced deviation from a rectangular shape in highly-loaded electrodes.

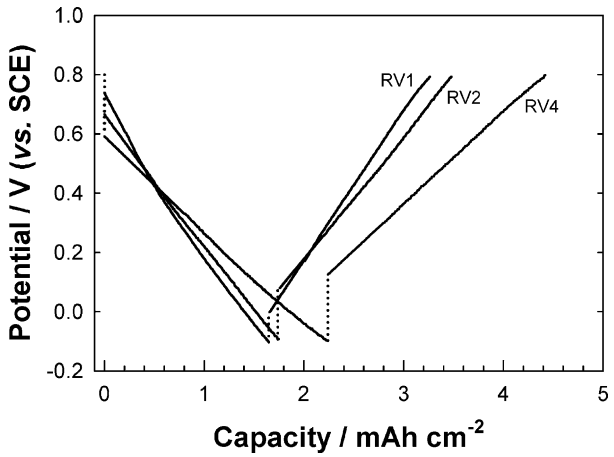

Fig. 8. Galvanostatic charge–discharge voltage profiles observed at 5 mA cm^{-2}. Note ohmic voltage drop at very early period of charge–discharge switching.

on Fig. 8 reveals that the ohmic voltage drop, which must be proportional to the ESR, becomes larger with increase in ruthenium loading. Given that the electrode resistance of the three electrodes is controlled to be the same and that the bulk electrolyte resistance is largely the same because an identical cell configuration was used, only the electrolyte resistance within pores differs for the three. Thus, the larger voltage drop (ESR) in the highly–loaded composite electrodes can be ascribed to a higher pore resistance. A relevant observation was made by Yoon et al. [2], whereby, it was found that the pore resistance is dominant compared with the electrode resistance or bulk electrolyte resistance. It was also found that carbons with smaller pores exhibit a larger ESR due to hindered ionic motions in such pores.

3.3. AC impedance analysis

The increase in the *RC* time constant with ruthenium loading is further confirmed by ac impedance studies. The Nyquist plot for the RV4 electrode is presented in Fig. 9a. When the spectrum is traced from the low-to the high-frequency range, the capacitive characteristic is observed as a vertical line below 50 mHz, followed by a sloped line (∼60°) from 50 to 100 Hz. Over 100 Hz, a depressed semicircle appears, which represents a parallel combination of resistive and capacitive components.

In order to compare the *RC* time constant for the composite electrodes, the frequency-dependent capacitance was obtained by taking the real part of complex capacitance, $C^*(f) = 1/(i\,2\pi f Z^*(f))$, where i, f and $Z^*(f)$ are the imaginary unit, ac frequency and complex impedance at a frequency, respectively [29–31]. The frequency-dependent capacitances of the three electrodes, normalized to the lowest frequency (5 mHz) values, are plotted in Fig. 9b. The frequency-dependent capacitance of porous electrodes can be analyzed using the transmission line model, which was proposed by de Levie with an assumption that pores are uniform and cylindrical [32,33]. The parameter 'penetration depth', $l = 1/\sqrt{\pi f R' C'}$, is useful to understand the impedance behavior of porous electrodes, where R' and C' represent the pore resistance and pore capacitance per unit pore length, respectively. This equation reads that, when the ac frequency is sufficiently high for the penetration depth (l) to be smaller than the pore length (l_p) of porous electrodes, only the outer surface (near pore opening) is influenced by the ac voltage signal [34,35]. As a result, a small capacitance is observed because only a limited part of electrode surface is utilized as a capacitor. In the low-frequency extreme, where the condition $l > l_p$ holds, most of the pore surface is utilized as a capacitor and results in a maximum capacitance. Based on this discussion, the frequency-dependent capacitance shown in Fig. 9b can be explained. The transmission line model appears to be valid in the present electrode systems because the used carbon is mesoporous. As expected, the capacitance is minimal at the high frequency limit, whereas a maximum capacitance is observed at the low-frequency limit. A monotonous capacitance change is observed in the intermediate-frequency region.

The *RC* time constant can be compared for the three electrodes by analyzing the capacitance profiles in the intermediate-frequency region. To this end, it is first assumed that utilization of the pore surface, where the EDLC component of the carbon surface and the pseudo-capacitive hydrous ruthenium oxide are developed, is 100% at the low-frequency limit (5 mHz) but zero at the high-frequency limit. This assumption is made based on the relation between the penetration depth (l) and the pore length (l_p) of porous electrodes. Then, a dotted line is drawn in Fig. 9b, which corresponds to 50% utilization of pore surface, to determine the ac frequencies at the crossing points between the capacitance profiles and the dotted line. Finally, the relative $R'C'$ values are extracted using the above equation with the penetration depth (l) being assumed to be the same for the three electrodes. The latter assumption is based on the fact that the penetration depth (l) has a certain identical value to deliver 50%

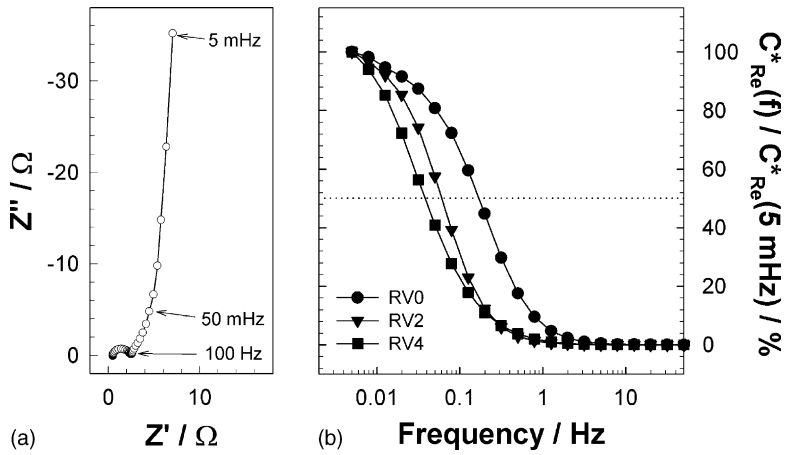

Fig. 9. (a) Typical Nyquist plot for RV4 electrode. Frequency range is 10^6 to 5×10^{-3} Hz. (b) Frequency-dependent capacitance profiles normalized to lowest frequency (5 mHz). Dotted line corresponds to 50% utilization of pore surface.

utilization of the pore surface for the three electrodes. The ac frequencies where the capacitance profiles and dotted line intersect are 0.170, 0.060 and 0.038 Hz for RV0, RV2 and RV4, respectively. From this, the *RC* time constants of the loaded electrodes are calculated to be 2.8 (RV2) and 4.4 (RV4) times higher than that of the unloaded electrode (RV0).

4. Conclusions

The prime concern in this work is to examine the extent of ruthenium utilization and to analyze the variation of rate capability (i.e. *RC* time constant) as a function of ruthenium loading. The following observations have been made.

(i) A different amount of metallic ruthenium is loaded on to a mesoporous carbon using a chemical vapor impregnation method. The pore structure of mesoporous carbon is not substantially changed with ruthenium loading. Nevertheless a slight but apparent pore narrowing is observed for the loaded samples.

(ii) The total specific capacitance is increased to 243 F g^{-1} by the additional pseudo-capacitance exerted by hydrous ruthenium oxide. The utilization of ruthenium as the pseudo-capacitor becomes poorer with increasing ruthenium loading. For samples with higher loading, only the surface region of the ruthenium particles is utilized as a pseudo-capacitor due to a larger particle size and an incomplete conversion to the pseudo-capacitive hydrous ruthenium oxide.

(iii) The rate capability of loaded electrodes decreases with ruthenium loading due to an increase in the *RC* time constant. An increment in ESR is observed in the charge–discharge potential profiles.

(iv) The frequency-dependent capacitance observed in ac impedance spectra can be explained by the transmission line model. Here, an increase in the *RC* time constant with ruthenium loading is further verified.

Acknowledgements

This work was supported by Korea Science and Engineering Foundation via Research Center for Energy Conversion and Storage.

References

[1] B.E. Conway, Electrochemical Supercapacitors, Kluwer Academic Publishers, Dordrecht, 1999.
[2] S. Yoon, J. Lee, T. Hyeon, S.M. Oh, J. Electrochem. Soc. 147 (2000) 2507.
[3] E. Frackowiak, F. Beguin, Carbon 39 (2001) 937.
[4] S.T. Mayer, R.W. Pekala, J.L. Kashmitter, J. Electrochem. Soc. 140 (1993) 446.
[5] R. Saliger, U. Fisher, C. Herta, J. Fricke, J. Non-Cryst. Solids 225 (1998) 81.
[6] C. Lin, J.A. Ritter, B.N. Popov, J. Electrochem. Soc. 146 (1999) 3639.
[7] J. Zhang, D. Jiang, B. Chen, J. Zhu, L. Jiang, H. Fang, J. Electrochem. Soc. 148 (2001) A1362.
[8] M. Ramani, B.S. Haran, R.E. White, B.N. Popov, J. Electrochem. Soc. 148 (2001) A374.
[9] M. Ramani, B.S. Haran, R.E. White, B.N. Popov, L. Arsov, J. Power Sources 93 (2001) 209.
[10] J.P. Zheng, Electrochem. Solid-State Lett. 2 (1999) 359.
[11] Y. Sato, K. Yomogida, T. Nanaumi, K. Kobayakawa, Y. Ohsawa, M. Kawai, Electrochem. Solid-State Lett. 3 (2000) 113.
[12] J.P. Zheng, P.J. Cygan, T.R. Jow, J. Electrochem. Soc. 142 (1995) 2699.
[13] J.M. Miller, B. Dunn, T.D. Tran, R.W. Pekala, J. Electrochem. Soc. 144 (1997) L309.
[14] R. W Pekala, J.C. Farmer, C.T. Alviso, T.D. Tran, S.T. Mayer, J.M. Miller, B. Dunn, J. Non-Cryst. Solids 225 (1998) 74.
[15] J.M. Miller, B. Dunn, Langmuir 15 (1999) 799.
[16] C. Lin, J.A. Ritter, B.N. Popov, J. Electrochem. Soc. 146 (1999) 3155.
[17] S. Han, T. Hyeon, Chem. Commun. (1999) 1955.
[18] S. Hadzi-Jordanov, H. Angerstein-Kozlowska, M. Vukovic, B.E. Conway, J. Electrochem. Soc. 125 (1978) 1471.
[19] D. Michell, D.A.J. Rand, R. Woods, J. Electroanal. Chem. 89 (1978) 11.
[20] V. Birss, R. Myers, H. Angerstein-Kozlowska, B.E. Conway, J. Electrochem. Soc. 131 (1984) 1502.
[21] K. Kinoshita, Carbon: Electrochemical and Physicochemical Properties, Wiley, New York, USA, 1988, pp. 187–193.
[22] H. Marsh, K. Kuo, in: H. Marsh (Eds.), Introduction to Carbon Science, Butterworths, London, 1989, p. 134.
[23] T. Zheng, Q. Zhong, J.R. Dahn, J. Electrochem. Soc. 142 (1995) L211.
[24] M.L. Green, M.E. Gross, L.E. Papa, K.J. Schnoes, D. Brasen, J. Electrochem. Soc. 132 (1985) 2677.
[25] J. Crosby, R.S. Hanley, US Patent 4,250,210 (1981).
[26] K. Kinoshita, Carbon: Electrochemical and Physicochemical Properties, Wiley, New York, USA, 1988, p. 299.
[27] M. Muller, B. Kastening, J. Electroanal. Chem. 374 (1994) 149.
[28] A.J. Bard, L.R. Faulkner, Electrochemical Methods: Fundamentals and Applications, Wiley, New York, USA, 1980, pp. 11–15.
[29] K. Honda, T.N. Rao, D.A. Tryk, A. Fujishima, M. Watanabe, K. Yasui, H. Masuda, J. Electrochem. Soc. 148 (2001) A668.
[30] J. Rishpon, S. Gottesfeld, J. Electrochem. Soc. 131 (1984) 1960.
[31] S.H. Glarum, J.H. Marshall, J. Electrochem. Soc. 129 (1982) 535.
[32] R. de Levie, Electrochim. Acta 8 (1963) 751.
[33] R. de Levie, in: P. Delahay (Eds.), Advances in Electrochemistry and Electrochemical Engineering, vol. VI, Interscience, New York, USA, 1967, p. 329.
[34] H.-K. Song, Y.-H. Jung, K.-H. Lee, L.H. Dao, Electrochim. Acta 44 (1999) 3513.
[35] H.-K. Song, H.-Y. Hwang, K.-H. Lee, L.H. Dao, Electrochim. Acta 45 (2000) 2241.